

Civilian Vehicle Radar Data Domes

Kerry E. Dungan^a, Christian Austin^a, John Nehrbass^b, Lee C. Potter^a

^aDept. of Electrical & Computer Engineering, The Ohio State University, Columbus, OH;
^bHigh-Performance Technologies, Inc., Centerville, OH

ABSTRACT

We present a set of simulated X-band scattering data for civilian vehicles. For ten facet models of civilian vehicles, a high-frequency electromagnetic simulation produced fully polarized, far-field, monostatic scattering for 360 degrees azimuth and elevation angles from 30 to 60 degrees. The 369 GB of phase history data is stored in a MATLAB file format. This paper describes the CVDomes data set along with example imagery using 2D backprojection, single pass 3D, and multi-pass 3D.

Keywords: SAR, 2D imaging, 3D imaging, scattering centers, sparse reconstruction

1. INTRODUCTION

In this paper, we describe a library of simulated X-band scattering data for civilian vehicles. For ten facet models, a high-frequency electromagnetic scattering code¹ was used to produce fully polarized far-field monostatic scattering with a bandwidth of 5.35GHz, for 360 degrees azimuth and elevation angles from 30 to 60 degrees. The viewing angles are depicted in Figure 1.

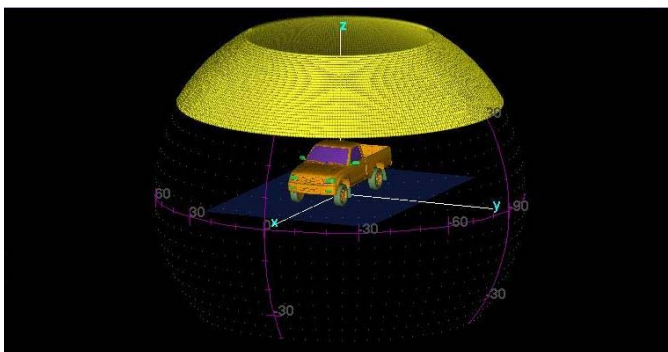


Figure 1. Visualization of elevation and azimuth angles used in computing simulated monostatic scattering. The viewing sphere is shown with a Tacoma CAD model.

2. CAD MODELS

The file names for ten modified facet files are listed in Table 1. Modifications to the original facet files are detailed in this section.

2.1 Ground Plane

The two-bounce multi-path returns from the ground and target contribute significantly to the observed returns in measured data. Therefore, it is important to include a ground plane in electromagnetic simulation of backscattered fields. For each CAD model, two facet files were created: one suitable for elevation angles no less than 30° and one for elevation angles no less than 44°. Note that the latter has a much smaller ground plane, resulting in an electrically smaller CAD object and shorter execution times.

An example of virtual dihedral returns from the ground plane and vehicle are visible in the MATLAB ray-tracing of a Ford Taurus SE facet model shown in Figure 2.

This technical paper has been approved for public release by the U.S. Air Force, document number 88 ABW-10-0975. Please send author correspondence to K.E.D. E-mail: dungan.2@osu.edu.

Vehicle	FileName.facet
Toyota Camry	CamryGnd30.facet
Honda Civic 4dr	HondaCivic4drGnd30.facet
1993 Jeep	Jeep93Gnd30.facet
1999 Jeep	Jeep99Gnd30.facet
Nissan Maxima	MaximaGnd30.facet
Mazda MPV	MazdaMPVGnd30.facet
Mitsubishi	MitsubishiGnd30.facet
Nissan Sentra	SentraGnd30.facet
Toyota Avalon	ToyotaAvalonGnd30.facet
Toyota Tacoma	ToyotaTacomaGnd30.facet

Table 1. Facet files for ten civilian vehicles; listed are files with ground plane sufficient for elevation angles no less than 30 degrees. A second set of files was created with smaller ground planes that supports elevation angles no less than 44 degrees; these additional files end in `Gnd44.facet`.

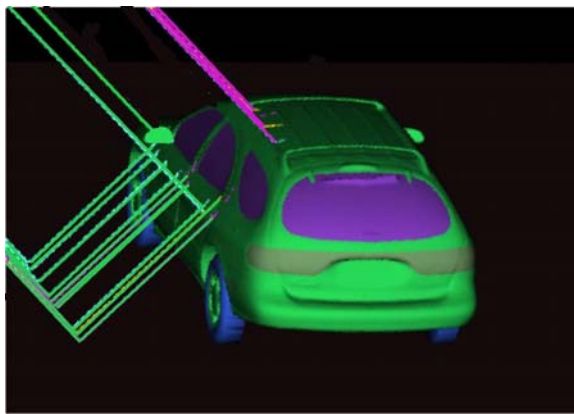


Figure 2. Visualization of ray tracing with Taurus wagon CAD model; visible at the bottom left are two bounce returns that significantly contribute to the target signature, especially at cardinal angles.

2.2 Material Labels

Material labels in the given CAD models were set to positive integers. Some material label numbers were modified from the original files; modifications are detailed below.

Many of the original CAD models contain interior components. Of the ten CAD models, seven contain facets with material label 80 to construct rough polygonal solids filling the vehicle interior. Such components are often used to absorb rays that enter the vehicle interior during simulation. The material label number for these facets was set to 200, for absorber. Of the ten CAD models, two contain facets with material label 208 for interior hard plastic components. The material label number for these facets was set to 200, for absorber. Finally, two models contain facets with material label 404 for interior seats. Likewise, the material label number for these facets was set to 200, for absorber. A summary of the interior facets is given in Table 2.

The integer labels selected for the modified facet files are given in Table 3.

3. MATERIAL PROPERTIES

The material label numbers define a material for each facet in the CAD models. The electrical and magnetic properties of the glass and asphalt are also defined. Below, we document selections for these properties.

3.1 Glass

For automotive glass, we chose to prohibit rays from entering into the vehicle interior, because the interior is not modeled in most facet files. This was accomplished with layered material and half-space backing (air, $\epsilon = \mu = 1$).

Vehicle	80 (fill)	208 (plastic)	404 (seats)
Toyota Camry			
Honda Civic 4dr	✓		✓
1993 Jeep	✓	✓	
1999 Jeep	✓		
Nissan Maxima			
Mazda MPV	✓	✓	✓
Mitsubishi	✓		
Nissan Sentra			
Toyota Avalon	✓		
Toyota Tacoma	✓		

Table 2. Several facet files among the ten civilian vehicles contain interior components; for use in the CVDomes data set, the material labels for all interior facets were set to 200 for absorber.

Material	Material
perfect electrical conductor (PEC)	0
rubber	200
glass	300
plastic	500
asphalt half-space	501
interior absorber fill material*	200
interior seats and plastic*	200

Table 3. Material numbers are integer labels to identify material types in a facet file. (An asterisk denotes that some, but not all, models include interior facets.)

This way, we get the correct reflection coefficient from the glass, but there is no transmitted ray into the interior of the CAD model.

For the glass layer,² thickness was approximated as 0.25 inch, $\epsilon = 5.9 - j0.15$ and $\mu = 1.0$. Note that high-frequency simulation code uses the $-j\omega$ sign convention; as a result, passive materials have negative imaginary parts for ϵ . The few plastic parts were assigned the same material properties as glass, acknowledging that the fidelity of the CAD models limits the utility of optimizing material selections. The material label number for rubber, 200, was identified as absorber. Finally, note that the code required material label 0 for perfect electrical conductor (PEC).

3.2 Asphalt

A brief review of the available literature yielded a representative model for the electric³ and magnetic⁴ properties: $\epsilon = 5.9 - j0.1$ and $\mu = 1.0008$. A mildly surprising similarity was found between reported ϵ values for glass and asphalt.

4. EM SIMULATION

Monostatic scattering was computed using a high-frequency electromagnetic (EM) simulation. For a triangular facet CAD model, the code uses geometric optics (shooting-and-bouncing rays) to induce currents, and then computes a physical-optics integral to generate electric field values in the far-field. The code supports material properties and provides an extrapolation capability for fast, approximate calculations. For the simulation parameters derived below, the extrapolation feature provides an acceleration in computation of approximately 75 – turning 11 weeks of CPU time into one day.

4.1 Input Parameters for Frequencies and Angles

Given the desired parameters in Table 4, we can derive all input parameters for the EM simulation.

Parameter	Value
Radar center frequency	9.6 GHz
Unambiguous range	≈ 15 m
Extrapolation extent	$\leq 0.25^\circ$
Azimuth extent	360°
Elevation extent	30° to 60°
speed of light	299792458 m/s

Table 4. Desired parameter values for high-frequency simulation of monostatic far-field scattering.

1. Shooting rays: rays are shot every $\delta = 0.5^\circ$, and the simulation extrapolates monostatic scattered fields $\pm 0.25^\circ$ using a point scattering approximation locally for a small sector in azimuth and elevation. The selection of $\pm 0.25^\circ$ extrapolation is an engineering judgment that balances scattering fidelity (at a level commensurate with the CAD precision) with accelerated execution. In this case, the extrapolation provides approximately 75 : 1 savings in execution time. Thus, each sector is a 0.5° -by- 0.5° region of azimuth and elevation samples for which monostatic scattering is approximated from a single ray tracing. The sectors tessellate the viewing sphere, keeping angular sampling constant, and adjacent sectors overlap at exactly one point on the boundary. These boundary points may be averaged to mitigate extrapolation discrepancy.
2. Angle sampling: We first select an odd integer K to yield approximately 15 meter unambiguous range. Computing at the center frequency of 9.6 GHz, we have

$$\frac{c/2}{2f_c \sin(\Delta\theta/2)} \approx 15m \Rightarrow \Delta\theta \approx \frac{1}{16.7^\circ}. \quad (1)$$

Thus, with a half-degree sector,

$$\frac{0.5}{K-1} \approx \frac{1^\circ}{16.7} \Rightarrow K \approx \frac{16.7^\circ}{2} + 1 = 9.35^\circ, \quad (2)$$

where K is the number of extrapolation samples. Hence, we choose $K = 9$ for approximately 15m unambiguous range and half-degree sectors. And, the resulting angular step size is

$$\text{step size} = \frac{0.5}{9-1} = \frac{1}{16} = 0.0625 \text{ degrees}. \quad (3)$$

Finally, this choice of angular step yields a 14.314 meter unambiguous range.

3. Sector size: For the required input parameter, we next determine ‘‘sector size.’’ The D -by- D angular sectors, when centered on quarter-integer {azimuth, elevation} pairs, should tessellate the sphere, keeping angular sampling constant (to within machine precision) and overlapping with the adjacent sector on the boundary. Thus, the extent (from first to last sample) of a sector is given by one-half degree.
4. Frequency sampling: we choose to select bandwidth and number of frequency bins so the down-range spatial frequency sampling matches the cross-range f_y frequency sampling, at the center frequency; this selection facilitates square-pixel imaging in the slant plane:

$$\begin{aligned} \Delta f_y &= 2f_c \sin(\Delta\theta/2) = 2 \cdot 9600 \sin\left(\frac{1}{16} \frac{1}{2} \frac{\pi}{180}\right) \\ &= 10.47197499276902 \text{ MHz}. \end{aligned} \quad (4)$$

Consequently, selecting $N = 512$ bins (511 steps) we have

$$\text{BW} = 511\Delta f_y = 5.351179221304969 \text{ GHz}. \quad (5)$$

The scattering code uses this figure in the units of inches, so we compute

$$\frac{c/2}{\text{BW}} = \frac{299792458/2 \text{ m/s}}{\text{BW}} \frac{100 \text{ cm/m}}{\text{Hz}} = \frac{100 \text{ cm/m}}{2.54 \text{ cm/in}} = 1.10282726377150 \text{ inches}.$$

Finally, the code defines “image size” as $N/2$ times this inches bandwidth, hence we obtain ± 282.3237795255046 inches for the square image extent.

These derived parameters required as input for the code are summarized in Table 5; MATLAB format is adopted for defining strings of numbers, and “Advance15” refers to the extrapolation option.

Input Parameter	Value
Radar center frequency	9.6 GHz
Azimuth centers	[0.25 : 0.5 : 359.75] degrees
Elevation centers, high	[44.25 : 0.5 : 59.75] degrees
Elevation centers, low	[30.25 : 0.5 : 43.75] degrees
Bandwidth	1.10282726377150 inches
Image size	± 282.3237795255046 inches
Frequency bins	512
Advance15: Angles per side	9
Advance15: Degree Span	0.5000000000000000 degrees

Table 5. Derived parameter values for high-frequency simulation of mononstatic far-field scattering.

4.2 Input Parameters for Shooting-and-bouncing Rays

The code accepts input parameters to define options in the implementation of the shooting-and-bouncing rays technique. Our selected settings are listed in Table 6. Note that the code does not allow an all-bounce contribution (PTD solution) when using a bulk material.

Input Page Section	Option Selected
#A File	Enter facet file name
#F Az and El	Script creates values for parallel jobs
#G center frequency	9.60 GHz
#G bandwidth DELZ	1.10282726377150inches
#G bandwidth DELX	1.10282726377150inches
#G bins	512
#G SAR image size	± 282.3237795255046 inches square
#H EM Settings	SBR on first bounce
#J SBR Settings: max. bounces	4
#J SBR Settings	10 rays per wavelength
#K Materials	“200” is the facet label for absorber
#K Materials	“2” \Rightarrow some parts are not PEC
#K Materials	insert materials into the input page
#Advance15 angles per side	9
#Advance15 degree span	0.5000000000000000

Table 6. Input page parameter values for high-frequency simulation of mononstatic far-field scattering.

5. HIGH-PERFORMANCE COMPUTING

The computational costs of the EM simulation are largely due to tracing of the shooting and bouncing rays (SBR). Because computing the results for a given set of azimuth and elevation angles is independent of computations from any other set, it would appear that massive parallelism is straightforward; however, when one attempts to scale simple computations over very large sets of processors, challenges often present themselves. These challenges and our corresponding solutions are discussed below. The computers used for this activity were sponsored by

the HPCMO. The details of the system used to run the EM simulation code are: 2048 Processors, 4 GB/Node, 4 TB Total, Infiniband Interconnect, 97 Terabyte Workspace, AMD Opteron (2.8 GHz). The HPCMO supplies these resources to a large customer base across the DoD and manages access via a queuing system. Over 72,000 CPU hours were required to complete the computations for this effort. With such a large investment, it was critical that the resource allocations were used in an efficient manner.

When a lab has total control of an HPC system, it becomes possible for several users to log on simultaneously and collectively process data. We attempt to provide this same capability in a shared environment and provide the ability to dynamically interface with the queuing system. A directory is identified for storing information about the computational tasks to be performed. For our purpose, the directory contains the lists of targets and angles. Permissions are set to allow collaboration. In this way, defining the list of tasks to be performed becomes independent of which user and/or which job actually computes these tasks. Additional tasks can be dynamically added without requiring a user to kill and restart jobs. If resources are already in use, a new task obtains real-time access to running resources. The outcome is that a queued systems behaves like an interactive system with exceptional efficiency.

For each target, a template input file was customized. A C-shell script created the required input files that spanned each angular sector (illustrated in Table 5) by simple string replacements from the template. The entire partial data dome consists of 86,400 files for each vehicle (both input and output files were saved). Each output file contains HH, HV, and VV linear polarizations with a complex-valued scattering coefficient at each frequency sample; 512 frequency samples span approximately 5.35 GHz bandwidth centered at 9.6 GHz. The output files provide a full circle of 720 azimuth sectors [0.25 : 0.50 : 359.75] for each of 60 sectors in elevation, [30.25 : 0.50 : 59.75]. Integers were used for a one-to-one mapping for the file convention. An integer value EL corresponds to an elevation angle of $30.25 + 0.50 * EL$, where EL has a valid range of [0 : 59]. Similarly, an integer value of AZ corresponded to an azimuth angle of $30.25 + 0.5 * AZ$, where AZ has a valid range [0 : 719]. After extrapolation of azimuth and elevation to 0.0625 angular sectors across the azimuth and elevation extents of [0°, 360°] and [30°, 60°], the data is processed and compressed into MATLAB files described in the next section.

6. MATLAB DATA FILES

Each data dome is stored as a set of elevation files with the file format `[vehicle]_el[elevation angle].mat`. For example,

`CamryGnd_el30.0000.mat`

stores the 360-degree phase history in a structure variable for the 30 degree elevation cut of the Toyota Camry. The data set contains elevations at 0.0625 degree intervals from 30 to 60 degrees. Each file contains a structure variable called `data`, where

```
data.azim is a vector of the azimuths in degrees;
data.hh, data.vv, data.hv are complex phase history arrays;
data.elev is the elevation angle in degrees; and
data.FGHz is a vector of frequencies in GHz.
```

The data is distributed by the Air Force Research Laboratory's SDMS at

<https://www.sdms.afrl.af.mil/main.php>.

Requests require a portable hard drive with a minimum formatted capacity of 369 GB; nominally 500 GB is sufficient.

7. SAMPLE IMAGING APPLICATIONS

The database of data domes provides the opportunity to generate images for a variety of simulated conditions. In this section, we provide a few example images that demonstrate some of the capabilities of the CVDomes database. These examples include simple 2D backprojection images along with single-pass and multi-pass 3D applications.

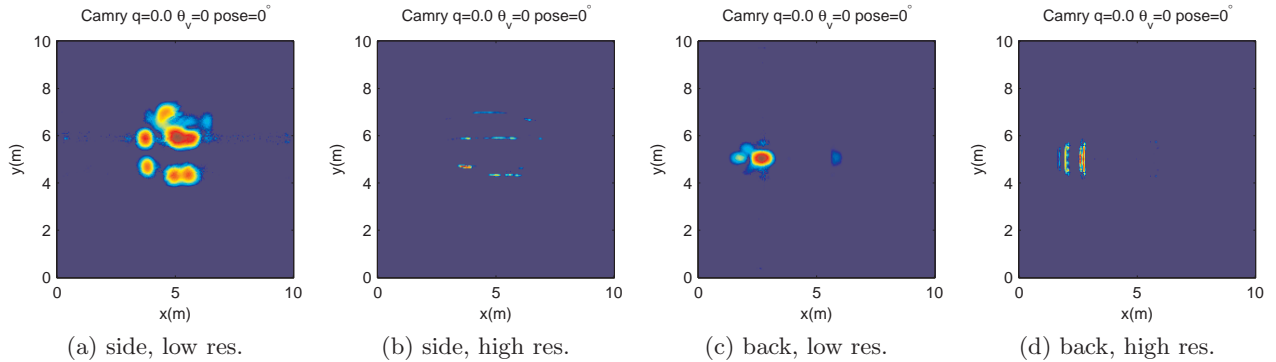


Figure 3. A Camry is imaged using 2D backprojection from the broad side in (a) and (b). The same vehicle is imaged from the back in (c) and (d).

7.1 2D Images

Given the available 360 degrees of aspect as well as the 30 to 60 degrees of elevation it is possible to generate images from a variety of perspectives and cross-range resolutions. Additionally, the database provides more than 5 GHz of bandwidth centered at 9.6 GHz; this allows for range resolution up to approximately 1.1 inches.

To demonstrate some of the imaging capability, we begin with images in Figure 3. Each image was generated using fast backprojection⁵ with data from a single elevation slice at 45 degrees from the left side and back of the Camry. With a radar center frequency of 9.6 GHz, the radar wavelength $\lambda = c/9.6e9 \approx 0.03m$. Thus the range and cross-range resolutions are given by⁶

$$\rho_{y'} = \frac{c}{2BW} \text{ and } \rho_{x'} = \frac{\lambda}{2\Delta\theta},$$

where x' and y' are referenced from the direction of the radar.

Figure 3a shows a magnitude image of the side of a Camry that uses 640 MHz of radar bandwidth and a four degree aperture, providing approximately $0.21m \times 0.23m$ resolution. When using 5 GHz of bandwidth and a 30 degree aperture, for approximately $0.03m \times 0.03m$ resolution, the side of the Camry is sharper as shown in Figure 3b. Similarly, Figures 3c and 3d show low and high resolution views of the Camry from the back.

By combining multiple images of a vehicle from different aspects, it is possible to gain some understanding of the vehicle's shape. Figure 4 shows four magnitude images that were generated from the coherent addition of complex 2D images. The individual subaperture images were taken from different azimuths stepped around the full 360 degrees of aspect using a nominal 45 degree elevation. If a vehicle were placed at the center of a circular SAR scene, as shown in Figure 4a, then the composite images for low and high resolution would look similar to those shown in Figures 4c and 4d respectively. For the 4 degree aperture low resolution images, individual images were repeated with a two degree overlap for a total of 180 images around the scene. Likewise for the 30 degree aperture high resolution images, individual images were taken every 15 degrees of aspect for a total of 24 images.

We also generated simulated 360 degree imagery for a vehicle that is rotated and offset from the scene center by $q = 0.4$ times the flight path radius, as described in Figure 4b. Figures 4e and 4f show the low and high resolution offset images, where each subaperture image uses a different elevation slice of the data dome that was determined from the geometry of the flight path to vehicle location.

The images in Figure 4 c-d show the typical characteristics of civilian vehicles in SAR imagery. Generally, there is an inner and outer ring of scattering. The inner ring shows the even bounce dihedral base of the vehicle with the ground, while the outer ring describes the odd bounce direct return from the elevated roofline.^{7,8} Given that these vehicles are sitting on a flat ground plane, elevated features are closer to the radar and are shown closer to the radar as imaged in 2D; this is the layover effect.⁶ The layover bulges in the offset imagery (Figure 4b) since the elevation angle is close to 60 degrees when the vehicle is closest to the radar and 30 degrees when farthest from the radar.

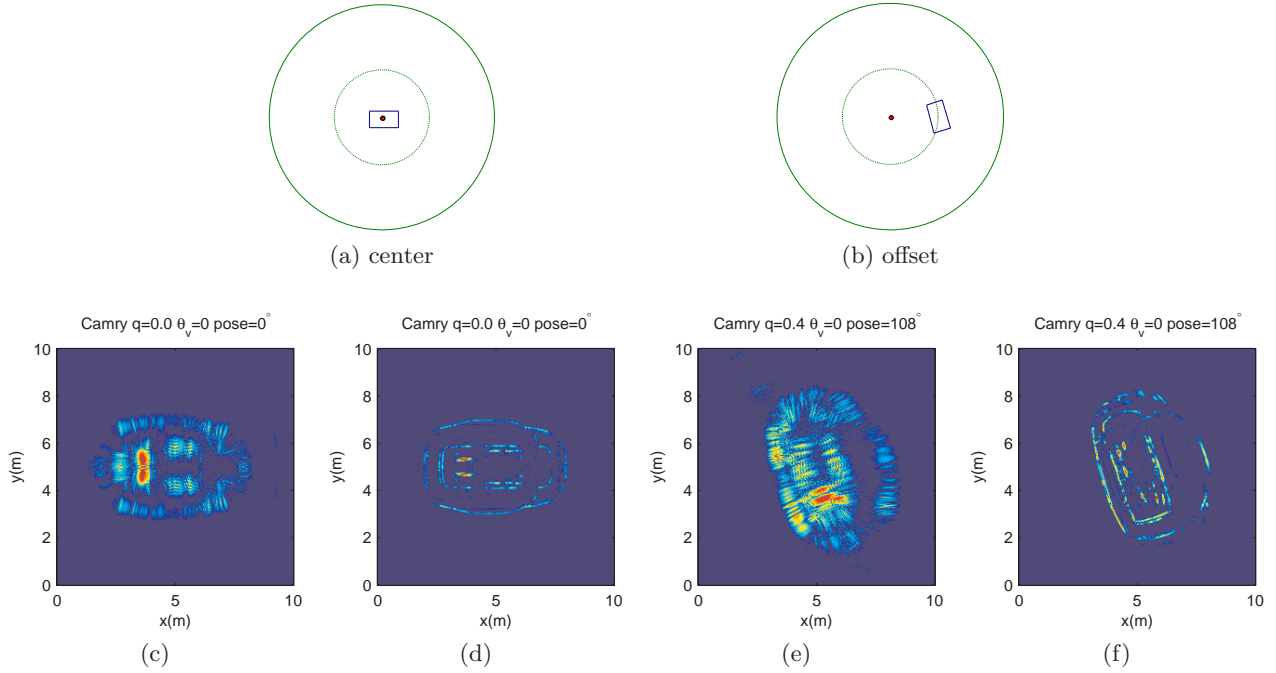


Figure 4. In a circular SAR scene, a Camry is sitting at the center (a) and offset from the center with a rotation (b). With 2D imaging from 360 degrees using a sequence of subaperture images, (c) and (e) show lower resolution images, while (d) and (f) show higher resolution images.

7.2 Attributed Scattering Centers and Single-pass 3D

Another method to visualize the vehicles of the CVDomes dataset is by extracting attributed scattering centers.⁸⁻¹¹ As with the imagery in Figure 4, we begin with wide-angle phase history processed as a sequence of subaperture 2D images using fast backprojection.⁵ A scattering center is found as a local peak in a magnitude image and is assigned attributes for 2D location, amplitude, polarization, azimuth angle, and elevation angle.⁸ Finally, we exploit layover and polarization to extract 3D location from the 2D images.⁸

To illustrate our application of attributed scattering centers, consider Figure 5, which shows three images of the same Camry using 640 MHz of bandwidth, 5 degree subapertures, and a constant 45 degree elevation. In

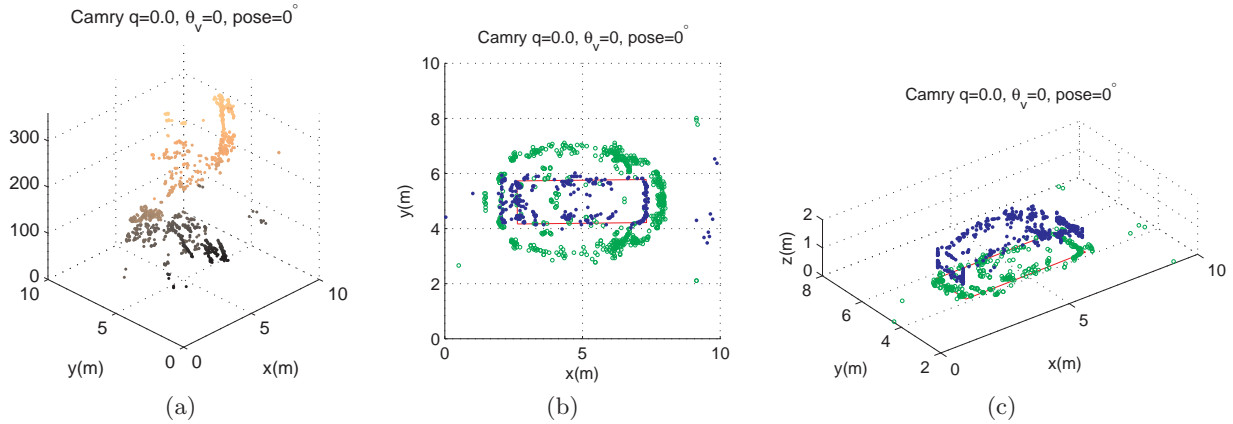


Figure 5. A Camry is imaged using attributed scattering centers. In (a) the azimuth attribute is shown along with the (x, y) location, while the even and odd-bounce attribute is shown in (b). A single-pass 3D image of the Camry is shown in (c).

Figure 5a the azimuth attribute is shown on the z-axis. A radar azimuth of zero degrees is imaged from the positive x direction, shown with dark colored points; as the azimuth angle increases counterclockwise around 360 degrees of aspect, the points are shown with a lighter shade. The leading edge of the vehicle forms a spiral pattern as azimuth increases.

Next, we adopt a binary attribute to record from which of two polarimetric images the peak was extracted: even-bounce or odd-bounce. The CVDomes dataset contains both HH and VV horizontal co-polarized and vertical co-polarized phase histories, respectively. The odd-bounce image is $HH + VV$, while the even-bounce image is $HH - VV$.¹²⁻¹⁴ Figure 5b shows a composite image of the (x, y) locations of all scattering centers for the Camry. The blue (dark) points represent the even-bounce scattering centers, and the green (light) points represent the odd-bounce scattering centers. Notice that the interior even-bounce scattering centers form a shape of the base of the vehicle, emphasized with the red rectangle, while the odd-bounce points are elevated points that layover in the direction of the radar.

Finally, Figure 5c shows a single-pass 3D image of the vehicle that was generated by inverting the layover of the suspected elevated points to positions above the base of the vehicle.⁸ For emphasis, the odd bounce scattering centers are shown with blue (dark) points, while the even scattering centers are shown with green (light) points.

7.3 Multi-pass 3D Reconstruction

Under a far-field operating scenario, the data collected across multiple passes provides a 3D annulus of k-space data, as opposed to a 2D annulus in k-space for a single pass collection. This third dimension of k-space data provides a third dimension of resolution in the image domain, without having to exploit prior knowledge of layover structure. Image reconstruction can be performed using direct 3D Fourier inversion methods.¹⁵ In practical collection scenarios, it may not be possible to fly enough passes to form sufficiently high resolution images using direct Fourier inversion methods. Images can be sharpened by utilizing the fact that radar images usually consist of a small number of large magnitude scattering centers. Sparse reconstruction algorithms use prior knowledge of scattering center sparsity by fitting a reconstructed image to collected k-space data, while penalizing for a large number of small scattering centers. Sparse reconstruction algorithms that solve the optimization problem

$$\hat{x} = \underset{x}{\operatorname{argmin}} \{ \|y - Ax\|_2^2 + \lambda \|x\|_p^p \} \quad (6)$$

have been applied to enhance radar images from different collection geometries.¹⁶⁻²⁰ In the sparse optimization problem, the measured phase history is y ; the reconstructed image is \hat{x} , and A is the Fourier operator; the p -norm $\|\cdot\|_p^p = \sum_{k=1}^K |x_k|^p$, $0 < p \leq 1$, and λ is a sparsity penalty weighting parameter.

The following multi-pass 3D images are formed from 72 non-overlapping 5 degree subapertures in azimuth covering the full 360 degree aperture; each of the subapertures include all of the passes, covering an elevation extent of $[30^\circ, 60^\circ]$, with a bandwidth of 640 MHz centered at 9.6 GHz is used. Samples in k-space are interpolated to a rectangular grid using nearest-neighbor interpolation to allow FFT implementation of the Fourier operator. The width of the grid is calculated as the edge width of the minimum bounding box that contains the subaperture at azimuth $[0^\circ, 5^\circ]$. Each of the subaperture images has a resolution of $0.038\text{m} \times 0.038\text{m} \times 0.038\text{m}$. Final wide-angle images are a non-coherent combination of the maximum magnitude voxel across all subaperture images. A more detailed discussion of this imaging processes can be found in Austin et al.^{19,20}

An example of multi-pass 3D imaging using direct Fourier inversion is shown at multiple angles for VV and HV polarizations in Figure 6 and 7. The interpolated data is inverted using an inverse FFT. All reconstructed points that are 30 dB below the maximum magnitude point are discarded from the image. If these points are included, the images are blurred and structure of the Camry is obscured. Blurring is a result of spreading of the image caused by limited k-space bandwidth.⁶

The structure of the Camry can be seen in the VV polarization images, although the features are not sharp. This structure cannot be seen in the HV polarization channel; there is some strong scattering in the rear of the Camry, but any additional structure cannot be seen in the dynamic range plotted.

When using a subaperture with a 5 degree extent in azimuth and a 30 degree extent in elevation, direct Fourier inversion is capable of generating good 3D reconstructed images, as shown in Figure 6. The benefits

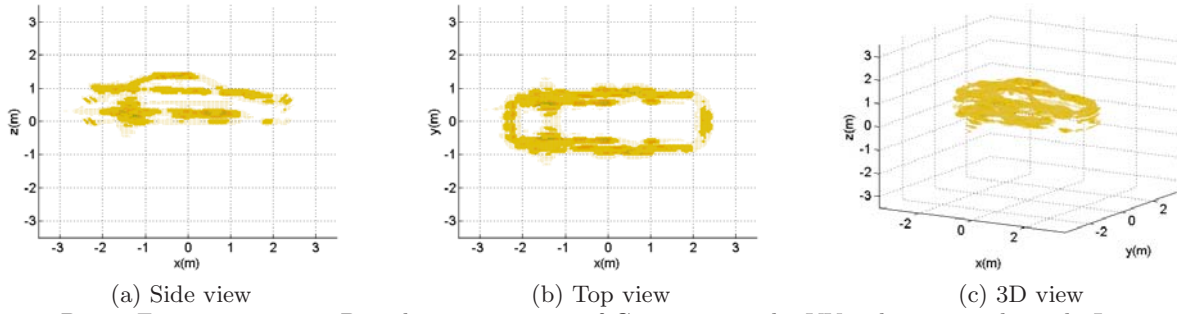


Figure 6. Direct Fourier inversion 3D multi-pass imaging of Camry using the VV polarization channel. Larger, darker points have larger magnitude and smaller, lighter points have smaller magnitude.

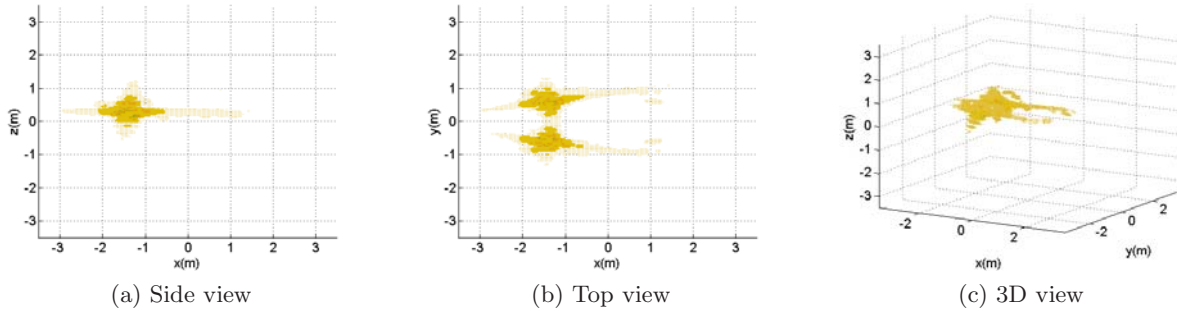


Figure 7. Direct Fourier inversion 3D multi-pass imaging of Camry using the HV polarization channel. Larger, darker points have larger magnitude and smaller, lighter points have smaller magnitude.

of sparse reconstruction with respect to direct Fourier inversion is most apparent when reconstructing images from low bandwidth k-space data, or non-linear flight geometries. However, it can still be used to sharpen the images formed using the bandwidth and multi-pass circular flight geometry considered here. Figures 8 and 9 show sparse reconstructed images for the VV and HV channels, respectively. The sparsity parameter $\lambda = 10$, and $p = 1$ in both images. The sparsity parameter is chosen qualitatively based on visual image quality. All reconstructed points that are 50 dB below the maximum point are discarded.

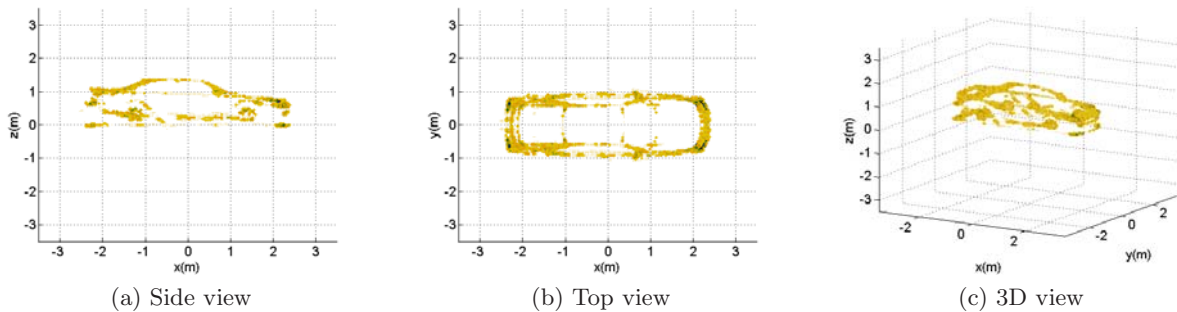


Figure 8. Sparse reconstruction 3D multi-pass imaging of Camry using the VV polarization channel. Larger, darker points have larger magnitude and smaller, lighter points have smaller magnitude.

Camry features are sharper in the sparse reconstructed images and a larger dynamic range of reconstructed scattering is displayed. For example, in the VV image, the roof outline is clear, and the rear-view mirrors can be seen; this is not the case in the direct Fourier images. Although the structure of the Camry can be seen in the top view of the HV image, the 3D reconstruction is inferior to the VV image. There are also some artifacts

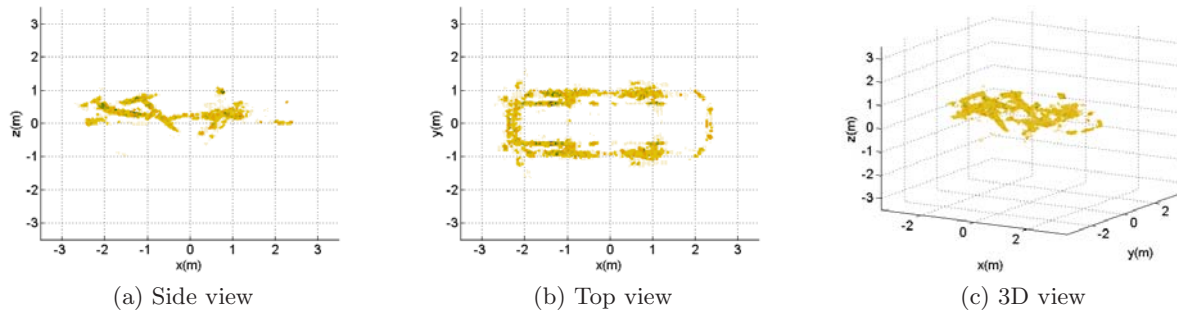


Figure 9. Sparse reconstruction 3D multi-pass imaging of Camry using the HV polarization channel. Larger, darker points have larger magnitude and smaller, lighter points have smaller magnitude.

in the HV image appearing as scattering below 0 m on the z-axis.

ACKNOWLEDGMENTS

This material is based upon work supported by the Air Force Research Laboratory under Award FA8650-07-D-1220 and by the Air Force Office of Scientific Research under Award FA9550-06-1-0324. Additional support for EM simulation was provided by SET Corp. Any opinions, findings, conclusions or recommendations expressed in this publication are those of the authors and do not necessarily reflect the views of the U.S. Air Force. The U.S. Government is authorized to reproduce and distribute reprints for Governmental purposes notwithstanding any copyright notation thereon.

REFERENCES

1. Gorham, L. A., Naidu, K. D., Majumder, U. K., and Minardi, M. A., "Backhoe 3d "gold standard" image," in *[Algorithms for Synthetic Aperture Radar Imagery XII]*, Zelnio, E. G. and Garber, F. D., eds., *Proc. SPIE* **5808**, 64–70 (2005).
2. University of Massachusetts Lowell, *Common radar materials and their scale model equivalents* (2009). Retrieved December 2009 from <http://stl.uml.edu/tools/scalemodel.html>.
3. Jaselskis, E. J., Grigas, J., and Brilingas, A., "Dielectric properties of asphalt pavement," *J. Materials in Civil Engineering* **15**, 427–434 (sep/oct 2003).
4. University of Tuebingen, *Geophysics working group* (2009). Retrieved December 2009 from <http://www.uni-tuebingen.de/geo/gpi/ag-appel/projekte/envmag/pollution/index.html>.
5. Gorham, L. A., Majumder, U. K., Buxa, P., Backues, M. J., and Lindgren, A. C., "Implimentation and analysis of a fast backprojection algorithm," in *[Algorithms for Synthetic Aperture Radar Imagery XIII]*, Zelnio, E. G. and Garber, F. D., eds., *Proc. SPIE* **6237**, 62370G (May 17 2006).
6. Jakowatz, Jr., C. V., Wahl, D. E., Eichel, P. H., Ghiglia, D. C., and Thompson, P. A., *[Spotlight-Mode Synthetic Aperture Radar: A Signal Processing Approach]*, Kluwer Academic Publishers, Norwell, MA (1996).
7. Jackson, J. A. and Moses, R. L., "Feature extraction algorithm for 3D scene modeling and visualization using monostatic SAR," in *[Algorithms for Synthetic Aperture Radar Imagery XIII, Proceedings of SPIE]*, Zelnio, E. G. and Garber, F. D., eds., **6237** (2006).
8. Dungan, K. E. and Potter, L. C., "Three-dimensional imaging of vehicles with wide-angle synthetic aperture radar," *IEEE Trans. Aerosp. Electron. Syst.* (accepted for publication).
9. Keller, J. B., "Geometrical theory of diffraction," *J. Opt. Soc. Amer.* **52**(3), 116–130 (1962).
10. Potter, L. C. and Moses, R. L., "Attributed scattering centers for SAR ATR," *IEEE Transactions on Image Processing* **6**(1), 79–91 (1997).
11. Dungan, K. E., Potter, L. C., Blackaby, J., and Nehrbass, J., "Discrimination of civilian vehicles using wide-angle SAR," in *[Algorithms for Synthetic Aperture Radar Imagery XV]*, Zelnio, E. G. and Garber, F. D., eds., *Proc. SPIE* **6970**, 69700Z (2008).

12. Giuli, D., "Polarization diversity in radars," *Proceedings of the IEEE* **74**, 245–269 (Feb. 1986).
13. Novak, L. M., Burl, M. C., and Irving, W. W., "Optimal polarimetric processing for enhanced target detection," *IEEE Trans. Aerosp. Electron. Syst.* **29**, 234–244 (Jan. 1993).
14. Ertin, E. and Potter, L. C., "Polarimetric classification of scattering centers using M-ary Bayesian decision rules," *IEEE Transactions on Aerospace and Electronic Systems* **36**, 738–749 (July 2000).
15. DeGraaf, S., "3-D fully polarimetric wide-angle superresolution-based SAR imaging," in [*Thirteenth Annual Adaptive Sensor Array Processing Workshop (ASAP 2005)*], MIT Lincoln Laboratory (June 7–8 2005).
16. Çetin, M. and Karl, W., "Feature-enhanced synthetic aperture radar image formation based on nonquadratic regularization," *IEEE Trans. on Image Processing* **10**, 623–631 (April 2001).
17. Ertin, E., Potter, L., and Moses, R., "Enhanced imaging over complete circular apertures," in [*Fortieth Asilomar Conf. on Signals, Systems and Computers (ACSSC 06)*], 1580–1584 (Oct 29 – Nov. 1 2006).
18. Kragh, T. and Kharbouch, A., "Monotonic iterative algorithms for SAR image restoration," in [*IEEE 2006 Int. Conf. on Image Processing*], 645–648 (Oct. 2006).
19. Austin, C. D. and Moses, R. L., "Wide-angle sparse 3D synthetic aperture radar imaging for nonlinear flight paths," in [*IEEE National Aerospace and Electronics Conference (NAECON) 2008*], 330–336 (July 16–18 2008).
20. Austin, C. D., Ertin, E., and Moses, R. L., "Sparse multipass 3D SAR imaging: Applications to the GOTCHA data set," in [*Algorithms for Synthetic Aperture Radar Imagery XVI*], Zelnio, E. G. and Garber, F. D., eds., SPIE Defense and Security Symposium (April 13–17 2009).